Effect of Oxidation Level on the Interfacial Water at the Graphene Oxide-Water Interface: From Spectroscopic Signatures to Hydrogen Bonding Environment

Rolf David,[†] *Aashish Tuladhar,*[§*] *Le Zhang,*[† †] *Christopher Arges,*[† †] *Revati Kumar* [†*]

[†]Department of Chemistry, Louisiana State University, Baton Rouge, LA 70803

[§]Physical Sciences Division, Physical and Computational Sciences Directorate, Pacific Northwest National Laboratory, Richland, WA 99352

[† †]Cain Department of Chemical Engineering, Louisiana State University, Baton Rouge, LA 70803

*E-mail: revatik@lsu.edu, aashish.tuladhar@pnnl.gov

ABSTRACT: The interfacial region of the graphene oxide (GO)-water system is non-homogenous due to the presence of two distinct domains: an oxygen-rich surface and a graphene-like region. The experimental vibrational sum-frequency generation (vSFG) spectra are distinctly different for the fully oxidized GO-water interface as compared to the reduced GO-water case. Computational investigations using *ab-initio* molecular dynamics were carried out to determine the molecular origins of the different spectroscopic features. The simulations were first validated by comparing the simulated vSFG spectra to experiment and the contributions to the spectra from different hydrogen bonding environments and interfacial water orientations were determined as a function of the oxidation level of the GO sheet. The *ab-initio* simulations also revealed the reactive nature of the GO-water interface.

TOC GRAPHIC:

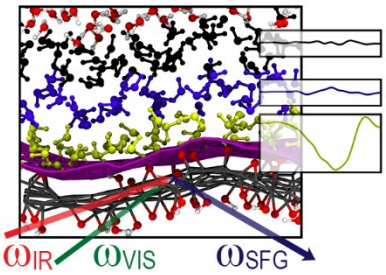

KEYWORDS: graphene oxide, AIMD, vSFG, hydrogen bonds, water network

I. INTRODUCTION

Graphene oxide (GO), single or a few layers of exfoliated sheets from graphite oxide, has recently received a lot of attention in the literature due to a range of potential applications.[1,2,11–20,3,21–30,4,31–35,5–10] GO consists of graphene sheets with oxygenated groups and a number of studies have revealed a wide range of oxygen-functional groups, such as hydroxyls and epoxides,[11] carboxylic acids, or sulfonates groups,[6,36] on these sheets as well as how these groups are arranged on the surface.[37–41] A key question that arises is how, depending on their number and partitioning, these oxygen-functional groups can favor or prohibit reactions at the GO-liquid interface in aqueous media. To probe interfaces, several surface-specific techniques can be used such as Environmental Scanning Electron Microscopy (ESEM), Secondary Ion Mass Spectrometry (SIMS), Auger Electron Spectroscopy (AES), etc.[42–46] One method, vibrational sum-frequency generation (vSFG)[47,48], has received a lot of attention for characterizing interfaces experimentally[49–57] and in conjunction with simulations.[51,52,58–62] The synergy between vSFG experiments and molecular simulations allows for an in-depth probing of the interface, permitting a finer molecular interpretation of the underlying interfacial region. In this paper, an analysis of the graphene-oxide-water interface by *ab-initio* molecular dynamics (AIMD) at different levels of oxidation has been carried out to provide insight on the effect of the different structural domains of graphene-oxide (organic, aromatic rich regions versus oxygen-rich hydrophilic regions) on the interfacial water structure. Furthermore, the effect of the oxidation level of the GO sheet on the water structure has also been studied. These results are put into perspective with the experimental vSFG spectra of these systems as a function of oxidation level, thereby not just confirming the accuracy of said *ab-initio* methods, but also providing insight into the molecular origins of the spectral signatures in the experimental vSFG spectra. This paper is divided into four sections. Both

the computational and experimental methods are outlined in Section II, the results are described and discussed in section III and the conclusions are presented in Section VI.

II. MATERIALS AND METHODS

a) *ab-initio* MD setup

The graphene-oxide (GO) sheets in this study consist of a single layer composed of 180 carbon atoms (to have an approximate 22.0 Å x 21.2 Å graphene sheet) and a varying number of oxygen-functional groups. The $GO_{4/1}$ and $GO_{2/1}$ sheets were constructed based on the work of Sinclair et al.[41] The former consists of 24 epoxide groups and 20 hydroxyl groups for a ratio C/O of 4.09 for the former, while 50 epoxide groups and 40 hydroxyl groups were introduced for a ratio of C/O of 2.00 for the latter case. The GO/water interface was generated by adding 265 water molecules on one side of the GO sheet generating a solvent layer of a thickness of 20 Å using the packmol software.[63] Using the moltemplate software,[64] parameter files for both systems were created using the OPLS-AA[65] force-field for the GO sheet along with the SPC/E[66] force-field for water. A 70 Å thick layer of vacuum is added in the z-direction (direction perpendicular to the interface) for both sets of systems resulting in a box of dimensions 22.0 Å x 21.2 Å x 104.0 Å. All simulations were carried out using periodic boundary conditions (PBC). For the classical molecular dynamics simulations, long-range electrostatic interactions were evaluated using the PPPM[67] method based Ewald summation method with a cutoff of 12.0 Å, while the Lennard-Jones interactions used a simple cutoff at 12.0 Å. All water bonds and angles were constrained using the SHAKE algorithm[68]. An initial geometry minimization was performed followed by a 500 ps equilibration run (with a timestep of 0.5 fs) in the NVT ensemble with the temperature set to 300 K with a Nosé-Hoover thermostat[69,70] and a time constant of 50 fs^{-1}. A production run was carried

out in the same ensemble for 1 ns with a timestep of 0.5 fs. Snapshots were extracted every 200 ps, resulting in five snapshots for each system. For each snapshot, and for both systems, geometry optimization and cell relaxation were done using the CP2K[71,72] program with the L-BFGS algorithm.[73] The force evaluations were done at the DFT level with the revPBE[74,75] functional and the empirical D3[76] dispersion, with a DZVP-MOLOPT-SR[77] basis set and GTH pseudopotentials[78–80]. The *c* cell parameter was kept fixed at 70.0 Å, giving a vacuum layer 40.0 Å thick, and PBC were applied in all direction using a periodic Poisson solver for electrostatics. For each optimized geometry, a 25 ps long NVT simulation at 300 K with a time step of 0.5 fs was then carried out with the Canonical Sampling through a Velocity Rescaling (CSVR) thermostat[81] and a 100 fs^{-1}. The position and velocities were extracted every 1 fs and the first 5 ps of each trajectory were discarded as equilibration. The total sampling for both the $GO_{2/1}$ and $GO_{4/1}$ case was 100 ps (5 x 20 ps).

b) Preparation of the graphene oxide samples

Large area oligo-layered graphene oxide (GO) flake solution of concentration 5 mg mL^{-1} was purchased from NewMater™. Transparent sapphire circular disks with flat surfaces (surface roughness < 1.0 mm) were acquired from Meller Optics, Inc. These disks had an area of 20.27 cm^2 (diameter of 5.08 cm) and a thickness of 0.33 nm. To attain a conformal graphene flake layer onto the substrate, a diluted solution of GO flakes was prepared by mixing the 5 mg mL^{-1} graphene oxide with methanol and water with a weight ratio of 1:1740:100 (graphene oxide:methanol:water). The dilute solution was spin coated on to the transparent sapphire substrate at 3000 rpm for 45 seconds. Prior to the deposition of the solution on the substrate for spin coating, 1 psi of nitrogen flow was applied to the surface of the sapphire substrate

from near normal incidence. Two more identical samples were prepared, and these samples were treated thermally to reduce graphene oxide on the sapphire substrate. The thermal reduction of graphene oxide thin film was conducted at 300 °C in a nitrogen filled chamber for 10 minutes for one sample and 6 hours for another sample. The successful reduction of GO film was evident by the film color change and the vSFG results (*vide supra*). **Figure 1** depicts the scheme to prepare thin GO/rGO films on transparent sapphire substrates.

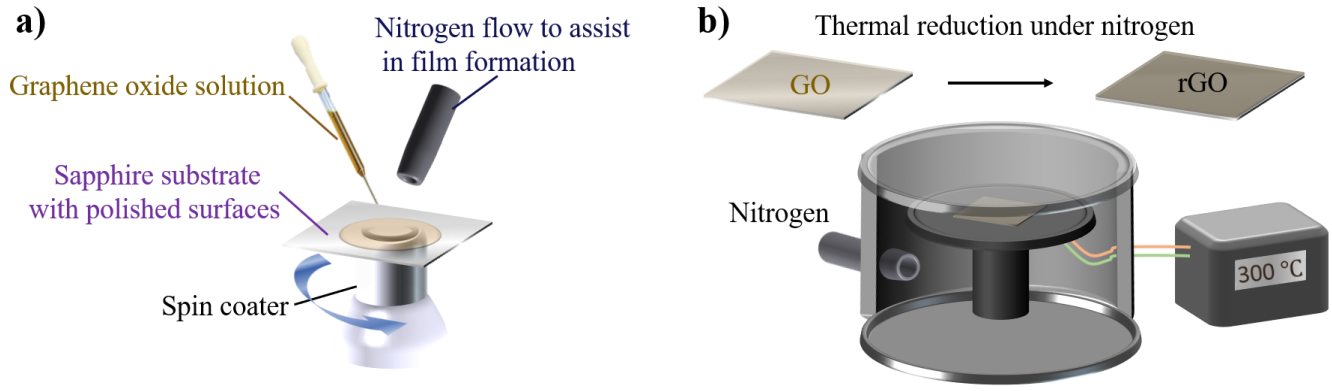

Figure 1: a) Spin coating process for preparing thin films of GO on transparent sapphire substrates with a polished flat surface. **b)** Thermal reduction of GO thin films to rGO in a thermal annealing chamber under nitrogen environment.

c) Experimental vSFG Setup

A picosecond scanning vibrational sum frequency generation (vSFG) spectrometer (EKSPLA, Lithuania), which has been described in previous works,[82,83] was used to perform vSFG experiments. Briefly, the vSFG spectrometer is a commercial setup that uses 532.1 nm visible beam and a tunable infra-red (IR) beam overlapped spatially and temporally at the sample surface. The angle of incidence is 35° and 31° for the visible and the IR beam, respectively. The spatial

resolution of the setup is ~6 cm^{-1}. An SSP polarization geometry (where S, S, and P refer to the polarization of sum frequency, visible, and IR photons, respectively) was used. In all experiments, each scan was obtained with an increment of 8 cm^{-1} and an average over 300 laser shots per point. The energy of the visible beam is typically about 200 μJ and that of the IR beam about 180 μJ. The SFG photons were detected using a high-gain low-noise photomultiplier (Hamamatsu R585) which is integrated into the Ekspla system. The voltage of PMT was set at 1400 V. The vSFG signal is normalized with respect to the visible and IR pulse energy.

The graphene oxide film grown on alumina substrate was placed in a pre-cleaned (thorough rinsing with detergent and copious amount of ion exchanged nanopure deionized water followed by drying with compressed N_2 and finally UV ozone cleaned (Novascan Technologies) for 15 minutes) home-built Teflon sample cell which was designed to allow for introduction of aqueous solution without moving the sample surface. Laboratory equilibrated deionized water (pH ~6) was used for the experiments. The schematic experimental geometry is shown in **Scheme S1** in the Supporting Information.

d) Surface-specific Velocity-Velocity Correlation Function from Simulations

In this study, the surface-specific Velocity-Velocity Correlation Function (ssVVCF) formalism proposed by Otho *et al*.[84] was used. The method is described in detail in Ref 84 and here just a brief description of the method is presented. In the case of just the IR spectrum, the IR response function (from the fluctuation-dissipation theorem) is related to the time derivative dipole-dipole correlation function.[85] The molecular dipole moment in turn is related to the permanent dipole moment of the molecule and the transition dipole moment of the normal mode,. The latter is determined by multiplying the transition dipole by the normal mode vector in the molecular frame.

Finally, the molecular dipole moment is converted to the lab frame through a rotational matrix that is applied to both the permanent and transition dipole moments in the molecular frame. The O-H stretch response is the one under consideration and can be considered to be decoupled from librational motion. The latter are dominated by the dynamics of the permanent dipole moment while the O-H stretch response by the transition dipole moment. Since the main contribution to the O-H stretch normal mode is the O-H vector,[86] the normal mode vector in the laboratory frame can be replaced by the bond vector resulting in a simplified description for the IR response to the O-H stretch that is proportional to the O-H stretch velocity autocorrelation function. A similar reasoning was applied by Otho *et al* for the SFG response function (which now also includes the polarizability tensor), connecting both the IR and SFG response to essentially different velocity-velocity type correlation functions.

$\chi_{xxz}^{(2),R}(\omega)$ is the resonant component of the second order susceptibility (z is the direction perpendicular to the interface) and can be written as:

$$\chi_{xxz}^{(2),R}(\omega) = \frac{Q(\omega)\mu(\omega)\alpha(\omega)}{i\omega^2}\chi_{xxz}^{ssVVCF}(\omega) \quad (1)$$

where $Q(\omega)$ is the harmonic quantum correction factor[87] and is given by :

$$Q(\omega) = \frac{\beta h\omega}{1 - e^{-\beta h\omega}} \quad (2)$$

with $\beta = \frac{1}{kT}$ and T is the temperature set to 300K.

The non-Condon effects were taken into account by the frequency dependent transition dipole moment and frequency dependent transition polarizability ($\mu(\omega)$ and $\alpha(\omega)$ respectively). parameterized in the work of Corcelli and Skinner,[88,89]

$$\mu(\omega) = \left(1.377 + \frac{53.03\ (3737.0 - \omega)}{6932.2}\right)\mu^0 \quad (3)$$

$$\alpha(\omega) = \left(1.271 + \frac{6.287\ (3737.0 - \omega)}{6932.2}\right)\alpha^0 \tag{4}$$

where ω, in (**Error! Reference source not found.**) and (**Error! Reference source not found.**), is specifically expressed in cm^{-1}

Finally, $\chi_{xxz}^{ssVVCF}(\omega)$ is given by:

$$\chi_{xxz}^{ssVVCF}(\omega) = \int_0^{\infty} dt e^{-i\omega t} \left\langle \sum_{i,j} g\left(r_{ij}(0)\right) \dot{r}_{z,i}^{OH}(0) \frac{\dot{\vec{r}}_j^{OH}(t) \cdot \vec{r}_j^{OH}(t)}{\left|\vec{r}_j^{OH}(t)\right|} \right\rangle \tag{5}$$

where i and j, are the i^{th} and j^{th} oscillators, respectively. $\dot{r}_{z,i}^{OH}$ is the *z* component of the velocity of the i^{th} oscillator, and $\dot{\vec{r}}_j^{OH}$ and $\vec{r}_j^{OH}$ are, respectively, the velocity vector and the displacement vector of the j^{th} oscillator. r_{ij} is the distance between the i^{th} center of mass and the j^{th} center of mass of the respective oscillators, and g(r) is a switching function:

$$g(r_{ij}) = \begin{cases} 1, r_{ij} \leq 2.0\ \text{Å} \\ 0, r_{ij} > 2.0\ \text{Å} \end{cases} \tag{6}$$

This switching function controls the cross-correlation terms between two oscillators: a r_{ij} cutoff at 2.0 Å, ensures only intramolecular coupling terms. The time correlation was evaluated for a t_{max} of 10 ps. A smoothing Hann window function, f(t) was applied to the Fourier transform of the time correlation function:

$$f(t) = \begin{cases} \cos^2\left(\frac{\pi t}{2\tau}\right), 0 < t < \tau \\ 0, t > \tau \end{cases} \tag{7}$$

The parameter τ was set to 0.50 ps.

Additional details including other switching functions that were used are given in the Supporting Information.

III. RESULTS AND DISCUSSION

a) Average water density fluctuations from the instantaneous water interface

In order to characterize the interface between the GO sheet and the water, the Willard-Chandler instantaneous interface[90] was employed as it provides a robust definition of the interfacial region. The ratio of the water density to the bulk density of water as a function of the distance to the instantaneous water interface is reported in **Figure 2**. Well-defined water layers, based on the minima in the density distributions in **Figure 2**, can be seen. This type of layering has also been seen for water next to other solid interfaces in studies carried out by Gaigeot et al.[91,92] In the $GO_{4/1}$ case three distinct layers of water, namely, L1, L2, and L3, with increasing distance from the instantaneous interface are seen. A fourth layer, L0, is only present in the case of $GO_{2/1}$, in the negative distance region (on the other side of the instantaneous interface) and corresponds to a small number of waters "trapped" on the GO sheet by the oxygen functional groups. Between the $GO_{2/1}$ and $GO_{4/1}$, the major difference for the density resides in the L1 layer, which is more structured for $GO_{4/1}$ due to a sharper peak, as well as the presence of an L0 layer solely in the case of $GO_{2/1}$.

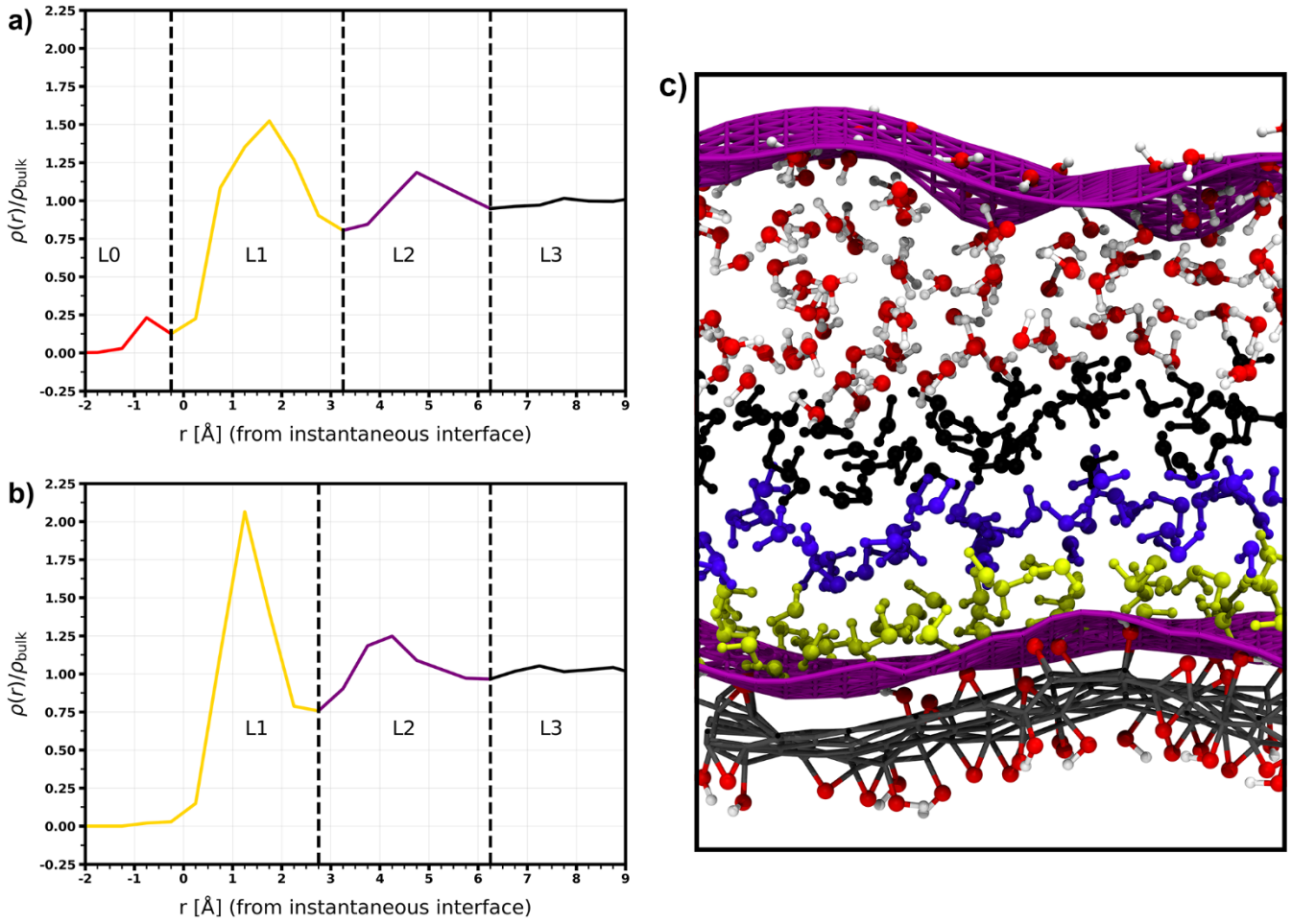

Figure 2: Ratio of the density of water over the bulk density of water as a function of the distance to the instantaneous water interface: **a)** for $GO_{2/1}$. **b)** for $GO_{4/1}$. **c)** Representation of the $GO_{4/1}$ system with the instantaneous water interfaces (in purple), the graphene oxide sheet, and the water layers. Water layers are yellow, purple, and black, representing L1, L2, and L3 respectively. (Carbon in grey, for waters beyond the L3 layer the oxygen atoms are in red and the hydrogen atoms are in white).

b) Hydrogen bond analysis of the interfacial waters

The hydrogen bond network of the waters was analyzed for both cases. A naming scheme for the different hydrogen bonding classes of water based on the work of Skinner *et al.*[93] was used

here. A water is defined as residing in a hydrogen-bonding class $\mathbf{N_a}$ where **N** is the total number of hydrogen bonds (see **Scheme S2** for definition of a hydrogen bond) a water molecule is involved in, and the subscript **a** refers to the number of hydrogen bonds involving the H atoms of the water under consideration: **a** is **S** for single donor water, **D** for double donor water, **T** and **Q** for triple and quadruple donor water, respectively. Water-water hydrogen bonds are considered as well as water-oxygen-bearing-groups hydrogen bonds. **Figure 3**, shows the percentage of hydrogen-bonding classes for all water within the L0 (**Figure 3a**) and L1 (**Figure 3b**) layers, for $GO_{2/1}$ and L1 layer for $GO_{4/1}$. The composition of the L0 layer is very different from the L1 layer, with the major class in L1 is $\mathbf{4_D}$ in L1 while $\mathbf{3_D}$ is the dominant hydrogen bonding configuration of waters in L0.

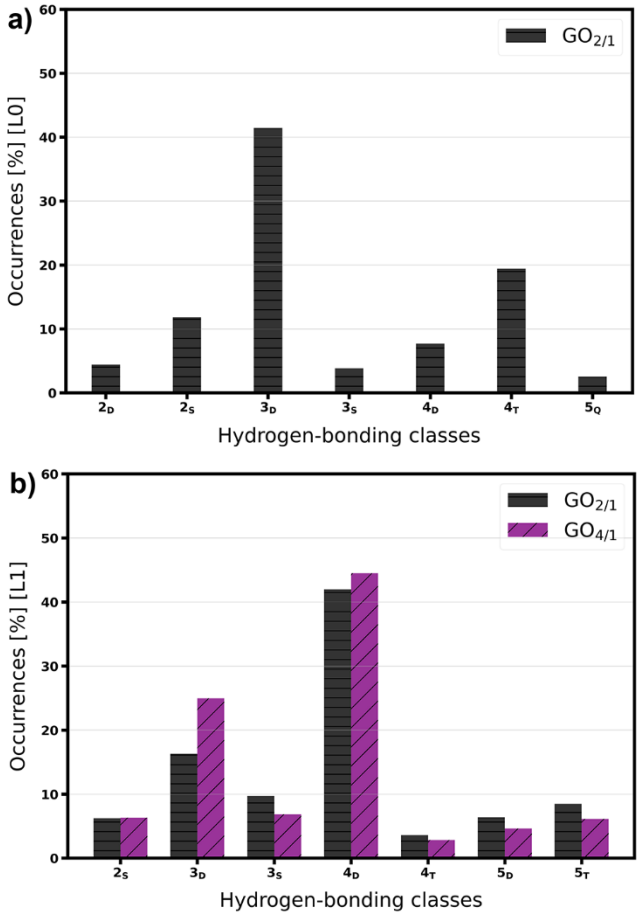

Figure 3: Distribution (in percentage) of the different hydrogen-bonding class of water. **a)** in the L0 layer for $GO_{2/1}$ (in black, horizontal stripes). **b)** in the L1 layers for $GO_{2/1}$ (in black, horizontal stripes) and $GO_{4/1}$ (purple, slanted stripes).

Although double donors are the most common in both L0 and L1, the waters in L0 tend to accept fewer hydrogen bonds. This point is reinforced by the second major class present in L0, namely, $\mathbf{4_T}$, which like $\mathbf{3_D}$ has only one acceptor hydrogen bond (The same goes for $\mathbf{2_S}$ and $\mathbf{5_Q}$). This can be explained by a specific orientation of the water molecule in this L0 layer, where a water oxygen is less readily accessible to other waters (or hydroxyl groups) to accept hydrogen bonds but its hydrogens are available to donate hydrogen point, a point which will be discussed further. Additionally, in this layer around 92% of the water molecules present are engaged in a hydrogen

bond with an oxygen-bearing group of the GO: this is due to a higher number of oxygenated defects and due to the "trapped" position of the water. Around 44% of these waters are both donating and accepting from an oxygen-bearing group.

For the L1 layer, compared to $GO_{4/1}$, $GO_{2/1}$ tends to have $GO_{2/1}$ with fewer $\mathbf{3_D}$ (-8.6 %) and $\mathbf{4_D}$ (-2.5 %) waters compared to $GO_{4/1}$, while a greater number of $\mathbf{3_S}$, (+2.9 %). Additionally, $GO_{2/1}$ has a larger percentage of waters with overall 4 or higher number of total hydrogen bonds that are double or triple donor ($\mathbf{4_T}$, +0.8 %, $\mathbf{5_D}$, +1.8 %, and $\mathbf{5_T}$, +2.4 %). Additionally, overall one can see an increase of single donors (+3.3 %) and triple donors (+4.0 %) at the expense of the double donors (-9.0 %). Between $GO_{4/1}$ and $GO_{2/1}$ there is an increase in the number of waters engaged in hydrogen bonds (donating or accepting) with an oxygen-bearing group (+6.4 %), the most increase comes from the waters accepting at least one hydrogen bond from an oxygen-bearing group (+9.8 %) or both accepting and donating one (+6.0 %). Compared to the L0 layer, in the L1 layer for $GO_{2/1}$, only 8.3 % of water are both accepting and donating to an oxygen-bearing group.

To summarize, the L1 layer, for both systems, has $\mathbf{4_D}$ as the major class with the second one being $\mathbf{3_D}$. $GO_{2/1}$ sees a small decrease in $\mathbf{4_D}$, and a bigger one in $\mathbf{3_D}$ but its number of highly hydrogen bonded water ($\mathbf{4_T}$, $\mathbf{5_D}$, $\mathbf{5_T}$) is greater than $GO_{4/1}$, due to an increase of waters engaged in hydrogen bonds (donating or accepting) with an oxygen-bearing group (+6.4 %).

c) Interfacial water orientation

To have a better understanding of the orientation of the water molecules around the interface between the graphene oxide sheet and water, the orientation of water molecules was examined. **Figure 4** shows the joint distribution of the θ_{DW}/θ_{HH} angles for water molecules in layer L1 for $GO_{2/1}$ (**Figure 4a**) and $GO_{4/1}$ (**Figure 4b**) and in layer L0 for $GO_{2/1}$ (**Figure 4c**), as well as the

definition of the two relevant angles chosen, θ_{DW} (**Figure 4d**) and θ_{HH} (**Figure 4e**). In the Supporting Information, the distribution for each trajectory is given and the results are shown to be consistent with the overall distribution (**Figure S1** and **Figure S2**).

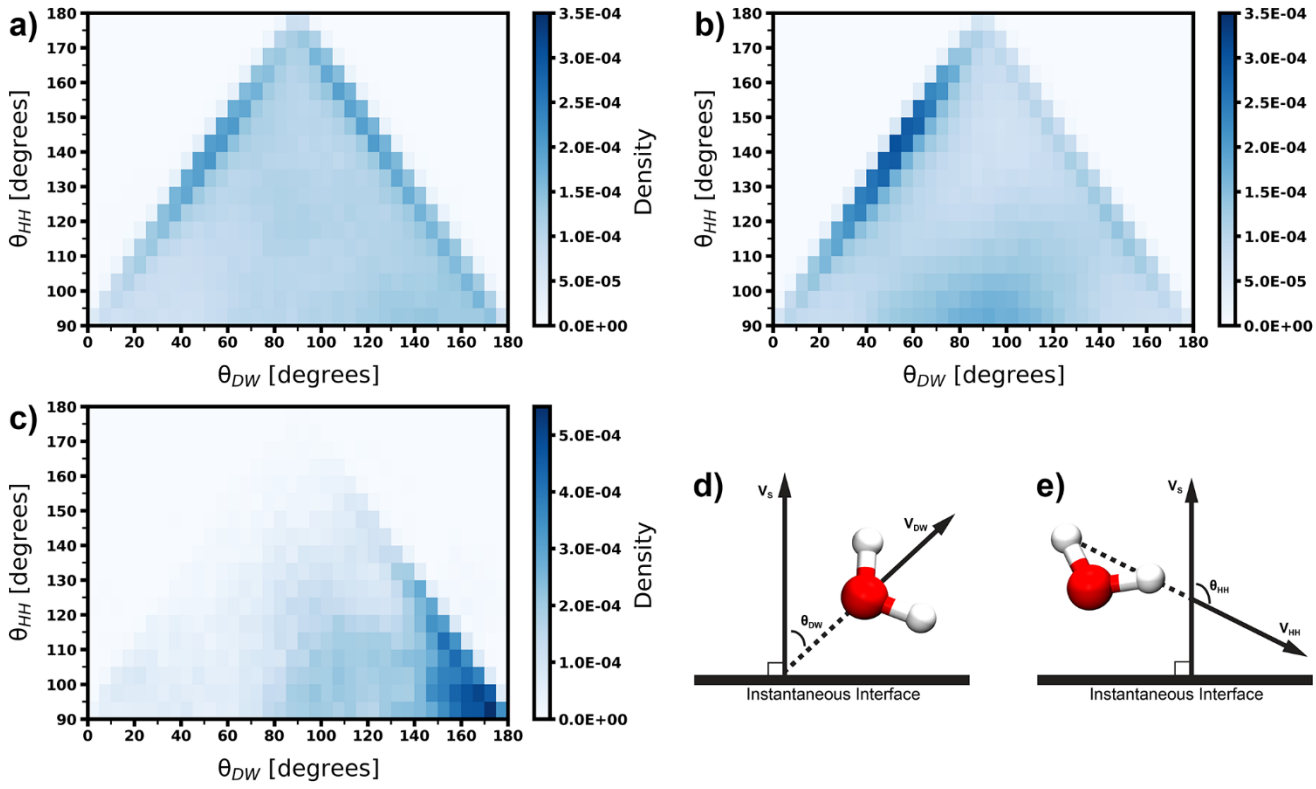

Figure 4: 2D histograms of the joint distribution of the θ_{DW} angle and the θ_{HH} angle for: **a)** $GO_{2/1}$ L1. **b)** $GO_{4/1}$ L1. **c)** $GO_{2/1}$ L0. **d)** Definition of the water orientation angle (θ_{DW}). V_{DW} is the water bisector and V_S is the vector normal to the instantaneous surface (always pointing in the direction of the water molecule). **e)** Definition of the water orientation angle (θ_{HH}). V_{HH} is the vector connecting the two hydrogen atoms of a water molecule vector and V_S is the vector normal to the instantaneous water surface (always pointing in the direction of the water molecule). All distributions were normalized to have unit area.

For the $GO_{2/1}$ L1 layer, two main orientations are present: one with values ranging from 50° to 55° and from 135° to 140° for θ_{DW} and θ_{HH} respectively corresponding to an orientation shown in

Figure 5a, with one hydrogen pointing away from the instantaneous interface. The second orientation ranges from 120° to 125° and from 140° to 145° for θ_{DW} and θ_{HH} respectively (**Figure 5b**), this time with a hydrogen pointing towards the instantaneous interface.

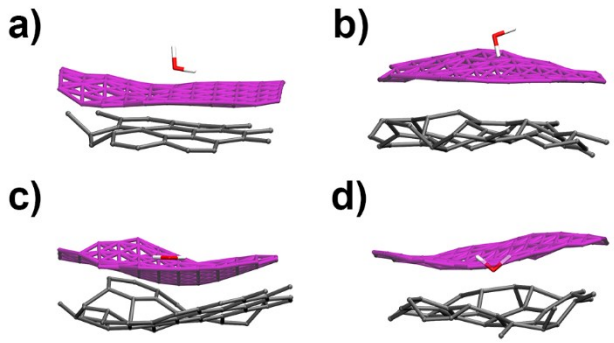

Figure 5: Selective geometries for characteristic θ_{DW}/θ_{HH} pairs. Only the carbons of the GO sheet are represented in grey for clarity, the instantaneous surface is represented in purple, the water molecule is represented in red for oxygen, white for hydrogens: **a)** θ_{DW}/θ_{HH} pair values equal to 50°/135° ($GO_{4/1}$ L1 and $GO_{2/1}$ L1). **b)** θ_{DW}/θ_{HH} pair values equal to 120°/140° ($GO_{2/1}$ L1). **c)** θ_{DW}/θ_{HH} pair values equal to 140°/90° ($GO_{4/1}$ L1). **d)** θ_{DW}/θ_{HH} pair values equal to 170°/90° ($GO_{2/1}$ L0).

For the $GO_{4/1}$ L1 layer, the distribution shows a major peak in the region from 50° to 55° for θ_{DW} and from 140 to 145° for θ_{HH} (a representative structure is shown in **Figure 5a**). A new minor peak is present around values ranging from 90° to 95° for both θ_{DW} and θ_{HH} (a representative structure is shown in **Figure 5c**), where both OH bonds are almost parallel to the instantaneous interface, slightly pointing towards it. The region with values from 145° to 150° and from 115° to 120° for θ_{DW} and θ_{HH}, respectively, is significantly diminished compared to $GO_{2/1}$. Finally, $GO_{2/1}$ presents the same number of OH bonds pointing away and towards the interface whereas, in $GO_{4/1}$, most of them are pointing away from the interface or are almost parallel to it.

For the $GO_{2/1}$ L0 layer, the joint distribution is shown in **Figure 4c**, and only one orientation is seen, with θ_{DW} ranging from 170° to 175° and a θ_{HH} value from 90° to 95° (**Figure 5d**). This configuration has both hydrogens pointing toward the instantaneous surface, which combined with the fact that in L0 water molecules are situated between the graphene sheet and the instantaneous interface, makes these hydrogens effectively pointing away from the graphene sheet.

d) vSFG spectra of the graphene oxide-water interface

As mentioned in the introduction, the vSFG spectroscopic technique is highly surface-specific due to its dependence on $\chi^{(2)}$, the second-order nonlinear susceptibility, and is thus zero in a centrosymmetric environment.[47,48] The experimental intensity (SSP polarization) $I_{ssp} \propto \left|\chi^{(2)}_{xxz}\right|^2$, where $\chi^{(2)} = \chi^{(2),R} + \chi^{(2),NR}$, with the two terms being the resonant ($\chi^{(2),R}$) and nonresonant ($\chi^{(2),NR}$) part, respectively. At a fixed visible frequency, the nonresonant term is constant.[94] However, it should be pointed out that there could be a small $\chi^{(3)}$ contribution to the experimental intensity,[95,96] which has been neglected in this work and will be examined in future work.

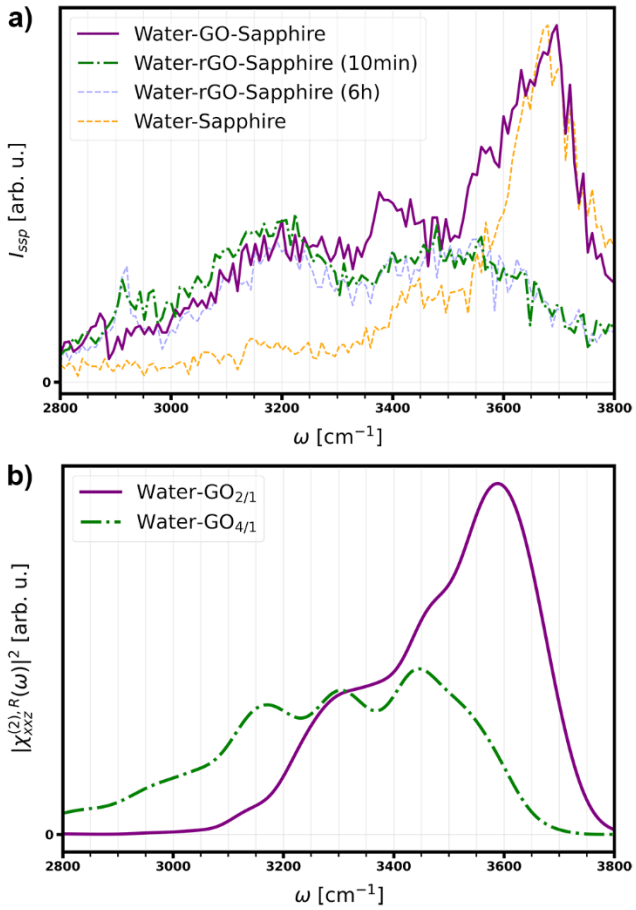

Figure 6: **a)** Experimental vSFG spectra of the water-graphene oxide interface before and after reduction by SSP polarization. **b)** Simulated vSFG spectra of the water-$GO_{2/1}$ and the water-$GO_{4/1}$ interfaces. The simulated spectra have been scaled to have the same height of the maximum as the experiment.

In **Figure 6a**, the experimental spectra of the water-graphene oxide-sapphire interface obtained by SSP polarization are reported. For the unreduced system, there is a major peak in the high-frequency region at 3700 cm^{-1} and a very broad intensity within the 3200-3500 cm^{-1} range with a minor peak at 3375 cm^{-1}. In the literature, this peak around 3700 cm^{-1} is typically attributed to dangling OH bonds pointing towards the air-water interface[50,53,59,97–99] or the graphene-water interface[100] whereas the range between 3200-3500 cm^{-1} is typically attributed to hydrogen-bonded

OH bonds (from water and hydroxyl groups) whether pointing away from or towards the interface.[50,53,59,97–99,101–103] After 10 min reduction, one can see the disappearance of the 3700 cm^{-1} peak, a growth of a peak around 3500 cm^{-1}, and a specific peak growing at 2900 cm^{-1} which can be attributed to methine groups resulting from the reduction of the graphene oxide.[104] After 6 hours of reduction, the system presents no major difference with the system after 10 min of reduction. One would expect that the more oxidized graphene oxide would present less high frequencies intensities at the interface due to the presence of more oxygen-bearing groups available for hydrogen-bonding, resulting in a lower number of weak or free OH oscillators: this is not the case, thereby underlining the need for molecular simulations of these two systems to obtain insight on the local structure of these interfaces.

A simulated spectrum can be obtained via the surface specific Velocity-Velocity Correlation Function (ssVVCF) formalism proposed by Otho et al[84] from molecular dynamics simulations. Here the resonant component of the second order susceptibility has been calculated. This method ensures a fast convergence, thus preventing the need for very long sampling trajectories. **Figure 6b** shows the simulated $\left|\chi_{xxz}^{(2),R}\right|^2$ spectra, where only the OH oscillators from the water (no contribution from GO hydroxyl groups) within 11 Å of the instantaneous interface (to avoid the other interface, namely the air-water present in the simulation) are taken into account. The simulated spectra with confidence intervals are given in the Supporting Information (**Figure S3**). The spectrum from the air-water interface can be found in **Figure S4** in the Supporting Information and reproduces the experimental spectrum of air-water interface from the literature, further validating the functional used in the AIMD simulations. These simulated systems, compared to the experimental one, possess no sapphire support for the graphene oxide sheet and any interpenetrated waters between the substrate and GO are absent.[100] For $GO_{2/1}$, the peaks are slightly

red-shifted (100 cm^{-1})[105] compared to the experimental results, with a major peak at 3600 cm^{-1} and a neighboring shoulder at 3300 cm^{-1}. Most of the low-frequency range (lower than 3200 cm^{-1}) is absent in the simulated vSFG spectra from $GO_{2/1}$. A possibility is that this region is different due to the non-inclusion of any OH bonds from any hydroxyl groups, which can form hydrogen bonds (and thus appearing in this low-frequency range) with other nearby oxygen-bearing groups (alkoxides, epoxides, hydroxyls) as well as water, as seen in previous experimental[106] and theoretical[107,108] vSFG studies on mineral-water interfaces. Nevertheless, the dominant features present in the experimental vSFG spectra are well represented. For the $GO_{4/1}$ case, the $\left|\chi_{xxz}^{(2),R}\right|^2$ shows the characteristic loss of the high-frequency dominant peak at 3600 cm^{-1}, consistent with the experimentally reduced GO, and gains three peaks at 3450, 3300 and 3150 cm^{-1} and a broad region below 3200 cm^{-1} which means that, for $GO_{4/1}$, OH bonds from water also account for this region suggesting a strong hydrogen-bonding environment not only due to hydroxyl groups. Once again, the simulated spectrum for $GO_{4/1}$ qualitatively reproduces the main features of the experimental vSFG spectrum. To get further insight into the interface, the resonant imaginary component, $Im_{\chi_{xxz}^{(2),R}}$, which is equal to $Im_{\chi_{xxz}^{(2)}}$ since typically the nonresonant part is real,[109] was examined. The sign of the imaginary part reflects the direction of the transition dipole (*i.e.* OH bond) with respect to the interface[109]: a positive sign for $Im_{\chi_{xxz}^{(2)}}$ correspond to a bond with the H atom pointing upward (away from the interface), and a negative sign, an OH bond with H pointing downward (toward the interface). **Figure 7a** and **Figure 7b** shows the imaginary component $Im_{\chi_{xxz}^{(2)}}$ for the $GO_{2/1}$ and $GO_{4/1}$ interfaces respectively, and the component for each layer is reported, corresponding to the depth from the interface, and as expected the L1 layer, in both systems, is the major contributing component to $Im_{\chi_{xxz}^{(2)}}$.

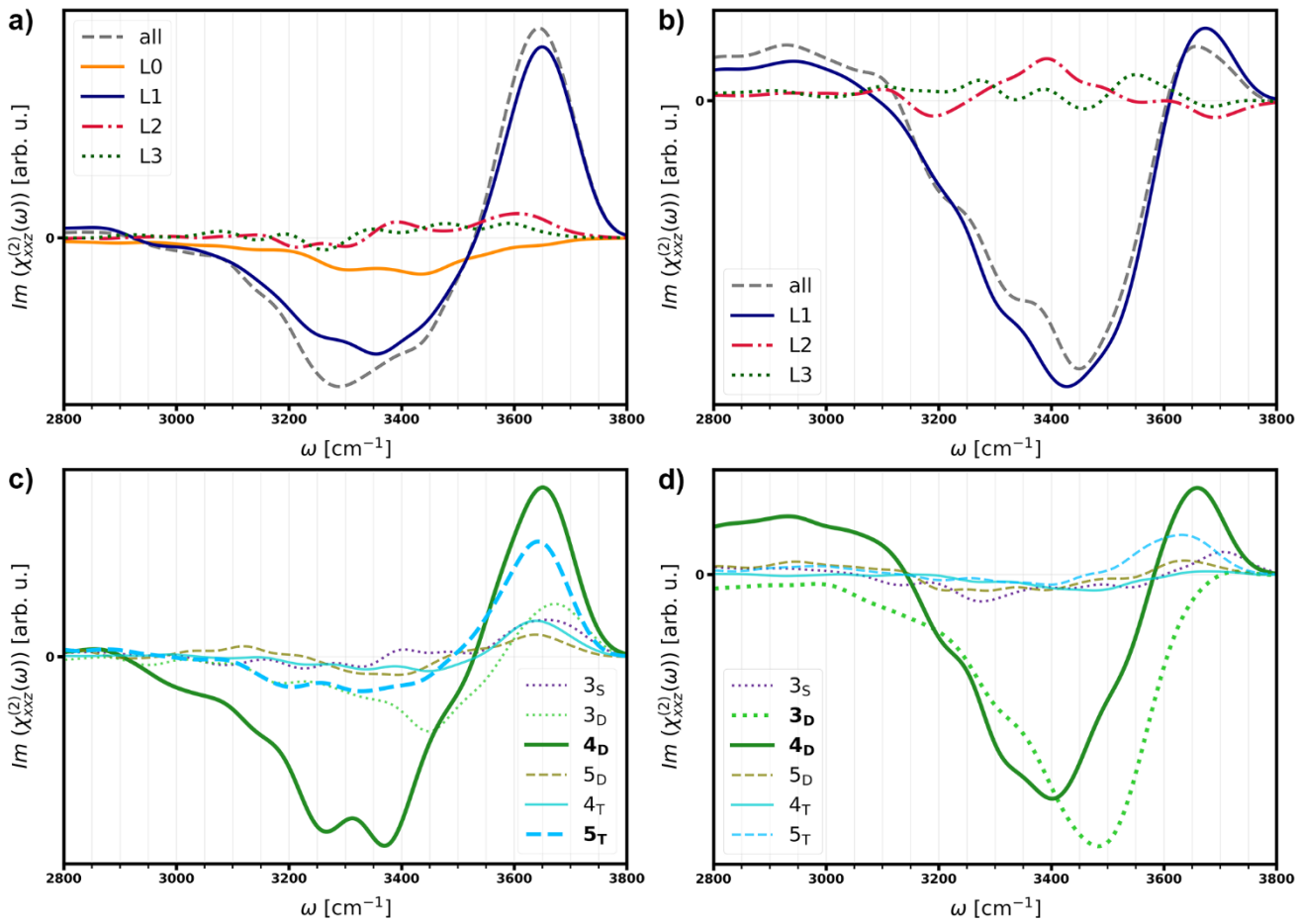

Figure 7: a) Imaginary part of the simulated vSFG spectra of the water-$GO_{2/1}$ interface by layers. **b)** The imaginary part of the simulated vSFG spectra of the water-$GO_{4/1}$ interface by layers. **c)** The imaginary part of the simulated vSFG spectra of the water-$GO_{2/1}$ interface within the L1 layer by hydrogen-bonding classes. **d)** Imaginary part of the simulated vSFG spectra of the water-$GO_{4/1}$ interface within the L1 layer by hydrogen-bonding classes.

For $GO_{2/1}$, the spectrum of the L0 layer has a negative broad region from ~3100 to ~3600 cm^{-1}. This is in keeping with the angle distribution in **Figure 4c**, where all water molecules are pointing away from the graphene-oxide sheet towards the instantaneous surface/interface. This broad negative range is consistent with **Figure 3a**, where the majority (80%) of water molecules are

double (or more) donors, presenting very few "free" or weakly hydrogen bonded OH bonds and are oriented away from the interface.

When looking at the L1 layer, $GO_{2/1}$ shows a negative region from ~3200 to ~3500 cm^{-1} and a sharper positive region at ~3600 cm^{-1}, which are in keeping with the angle distribution in **Figure 4a**, where the water presents both orientations: one with the water oriented with the H of the OH bond pointing away from the instantaneous interface (**Figure 5a**) thereby contributing to the negative region in the imaginary spectrum and another one with, this time, an OH bond with the H pointing towards (**Figure 5b**) the GO sheet and the instantaneous interface (contributing to the positive peak at higher frequencies).

For the L1 layer of $GO_{4/1}$ (**Figure 4b**), $Im_{\chi^{(2)}_{xxz}}$ presents a major broad negative peak centered at ~3400 cm^{-1}, a small positive peak at ~3700 cm^{-1} and a small positive component in the low frequency region (less than 3000 cm^{-1}). This is consistent with the angle distribution with most waters having an OH pointing away from the surface (**Figure 4b** and **Figure 5a**).

For further insight, $Im_{\chi^{(2)}_{xxz}}$ is reported in **Figure 7c** and **Figure 7d** for each major water hydrogen-bond class in the L1 layer for $GO_{2/1}$ and $GO_{4/1}$, respectively. The $\mathbf{4_D}$ class of water, which is the major class for both systems, gives rise to markedly different spectra in the two cases. Additionally, the other two hydrogen bonding classes that contribute to the spectrum of $GO_{2/1}$ are $\mathbf{3_D}$ and $\mathbf{5_T}$ whereas for the $GO_{4/1}$ case the only other major contribution apart from $\mathbf{4_D}$ waters is from the $\mathbf{3_D}$ waters.

The θ_{DW}/θ_{HH} joint distribution for the $\mathbf{4_D}$ waters in the L1 layer for the two GO interfaces (**Figure S5a** and **Figure S5b**) clearly shows a broad distribution for the $GO_{2/1}$ case while for the $GO_{4/1}$ case the waters are predominantly such that one OH bond points away from the interface with the other parallel to the interface (**Figure 5a**) with a minor peak with the waters almost

parallel to the interface but pointing slightly towards the interface. This is in keeping with the $Im_{\chi^{(2)}_{xxz}}$ spectra for the **4D** waters in the L1 layer which has large positive and negative contributions for the $GO_{2/1}$ case whereas the positive contribution is considerably dampened in the $GO_{4/1}$ case. The **3D** waters also show a broad distribution (**Figure S5c** and **Figure S5d**) for the $GO_{2/1}$ case whereas for the $GO_{4/1}$ the waters are oriented with one OH pointing away from the interface and the other parallel to the interface or a minor peak with waters almost parallel but pointing slightly away from the interface. This again reflects the features of the $Im_{\chi^{(2)}_{xxz}}$ spectra for the two interfaces with a positive and negative region for the $GO_{2/1}$ case but only a negative region for the $GO_{4/1}$ case. The **5T** case (**Figure S5e** and **Figure S5f**) has waters for both interfaces essentially oriented with one OH pointing towards the interface and the other parallel to the interface corresponding to an essentially strong positive feature in the spectrum.

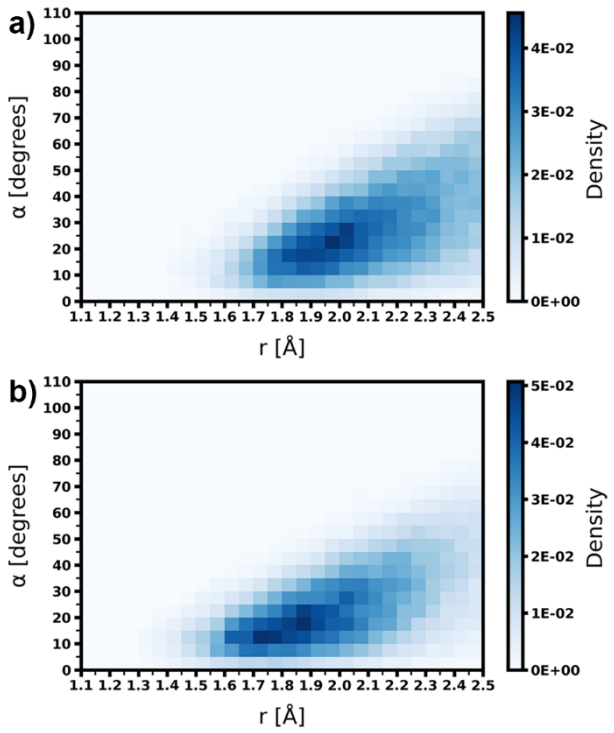

Figure 8: 2D histograms of the joint distribution of the r-α pair for hydrogen bonds with donating L1 **4_D** water (and where their distance to the instantaneous surface is less or equal to the first density peak, 1.75 Å for $GO_{2/1}$, 1.25 Å for $GO_{4/1}$). Only hydrogen bonds with the OH_D donor vector pointing towards the interface ($\theta_{OH} \geq 110°$) are considered. **a)** $GO_{2/1}$.**b)** $GO_{4/1}$. All distributions were normalized to have unit area.

Closer examination of the hydrogen bonds of the **4_D** waters that are within the first maxima of the L1 region (distance from the instantaneous surface is less than or equal to the first peak, 1.75 Å for $GO_{2/1}$, 1.25 Å for $GO_{4/1}$) show some interesting features (See Supporting Information for the definition of the r-α pair). For OH_D donor vectors pointing towards the interface ($\theta_{OH} \geq 110°$), the joint distribution of the hydrogen bond distance (r) and hydrogen bond angles (α) (**Figure 8a**) show significant deviation from the bulk water case (**Figure S6**) for $GO_{2/1}$ with larger angles and longer distances, suggesting that these hydrogen bonds are much weaker than the case of bulk

water and hence are much less red-shifted. This effect is less pronounced for the $GO_{4/1}$ case (**Figure 8b**) and coupled with the fact that these orientations are far fewer in the $GO_{4/1}$ case, the positive feature at high frequencies is considerably dampened.

From this decomposition analysis, one can see that in addition to the differences in the distribution of the hydrogen-bonding classes of water, the interfacial waters at the $GO_{2/1}$- and $GO_{4/1}$-water interfaces are oriented differently depending on the oxidation level of the graphene-oxide sheet resulting in very different vSFG spectra. The combined analysis of the orientation and hydrogen-bonding environment gives substantial insight into the type of interaction with water and the graphene-oxide surface. The $\mathbf{5_T}$ class, increasing only by 2.4 % between $GO_{4/1}$ and $GO_{2/1}$ and accounting for less than 10 %, becomes the second most dominant feature of the spectra for $GO_{2/1}$, and the $\mathbf{3_D}$ class decreasing from 24.9 % to 16.3 % in $GO_{2/1}$, still being the second most populous class, is not a dominant feature any more in the vSFG spectra. The $\mathbf{4_D}$ class, varying from 44.5 % to 42.0 %, drastically changes its contribution to the vSFG spectra between $GO_{4/1}$ and $GO_{2/1}$.

e) Reactivity of the GO-water interface

The AIMD simulations reveal several spontaneous epoxide (**Figure 9a**) opening events forming a charged pair of an alkoxide ion and a delocalized carbocation on the GO sheet (**Figure 9b**), highlighting the reactive nature of the GO surface. These alkoxides are further stabilized by hydrogen bonds from both the hydroxyl groups of GO and water, and **Figure S7** in the Supporting Information shows that the hydrogen bonds formed by water with the alkoxide are very strong (unlike the other oxygenated groups) leading to red-shifts in the OH spectra. The alkoxide ions can abstract a proton from a neighboring hydroxyl group forming a hydroxyl group and a new

alkoxide, resulting in the shuttling of the alkoxide along the sheet. Furthermore, reactive events in which the alkoxide extracts a proton from water forming a hydroxyl group are also seen (**Figure 9c**).

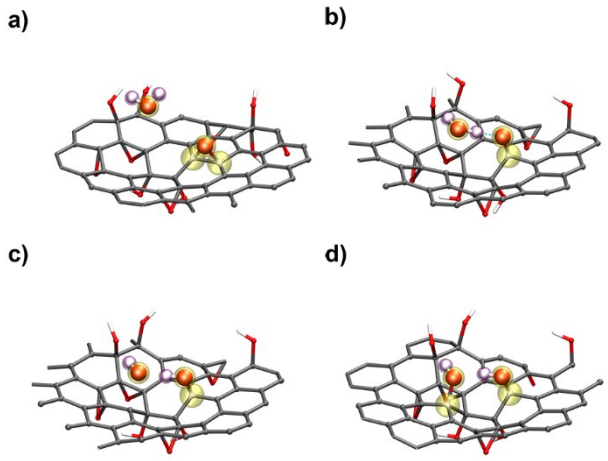

Figure 9: Reactive event chain in the $GO_{4/1}$: **a)** Epoxide and water **b)** Epoxide opening to form an alkoxy and a carbocation. **c)** Water hydrogen abstraction by the alkoxy to form a hydroxy group. **d)** Addition of the hydroxide (previously formed from the water) on the carbocation to form a new hydroxy group. Reactive species are highlighted and are represented with ball and sticks. The other part of the graphene oxide surface is represented with sticks. Only a portion of the GO sheet is shown with just the reactive water (the remaining waters and GO sheet are not shown for the sake of clarity). Carbons, oxygens, and hydrogens are represented in grey, red and white, respectively.

This could also be the origin of the positive red-shifted region in the water spectrum of $GO_{4/1}$ since the OH group of the reactive water has a partial hydroxyl group character. Interestingly, the decomposition of the imaginary spectrum of water O-Hs in the L1 layer that participate or do not participate in hydrogen bonds with the GO surface, shows that the O-H waters that are involved in hydrogen bonds (specifically donor hydrogen bonds) give rise to this red-shifted feature (see **Figure S8** and **Figure S9**) in $GO_{4/1}$. The hydroxide ion that is formed can then attack the

carbocation forming another hydroxyl group (**Figure 9d**). These ring-opening events that create alkoxide species result in carbocations that are stabilized by the graphene rich regions that are present in $GO_{4/1}$. Hence it is unsurprising that for $GO_{4/1}$, the ratio of alkoxide to oxygen-bearing groups is 0.066, and for $GO_{2/1}$, it is only 0.030 and hence reactive events are more likely in the $GO_{4/1}$ case due to the two separate domains. Future studies will further examine these reactive events.

IV. CONCLUSION

This paper demonstrates that the orientation and the hydrogen-bonding class of water molecules plays a major role in the vSFG spectra and sheds light on the interactions specific to this interface. The *ab-initio* MD simulations are in good agreement with the experiments, highlighting the fact that the DFT method used here is adequate for this system, and details how the water molecules are adapting to the different levels of oxidation of the graphene-oxide sheet. It also provides insight into the interpretation of experimental spectra at a molecular level. A highlight of this work is the fact that this surface is reactive, with epoxide opening and alkoxide shuttling as well as proton abstraction events from interfacial waters, which will be the focus of future studies.

ASSOCIATED CONTENT

Additional details and results for the hydrogen bond definition, details of the switching function used in the ssVVCF scheme, simulated air-water vSFG spectrum, joint angle distribution and joint hydrogen definition pair are given in the Supporting Information.

The Supporting Information is available free of charge on the ACS Publications website.

AUTHOR INFORMATION

Corresponding Author

*To whom correspondence should be addressed: revatik@lsu.edu, aashish.tuladhar@pnnl.gov

Author Contributions

All authors have given approval to the final version of the manuscript.

Notes

The authors declare no competing financial interests.

Rolf David Orcid ID: 0000-0001-5338-6267

Aashish Tuladhar Orcid ID: 0000-0003-2449-4984

Le Zhang Orcid ID: 0000-0002-0768-4850

Christopher Arges Orcid ID: 0000-0003-1703-832

Revati Kumar Orcid ID: 0000-0002-3272-8720

ACKNOWLEDGMENT

R.D. and R.K. acknowledge support from the National Science Foundation, grant number CHE-1845795, as well as LSU-HPC and LONI for computer time. A.T. acknowledges the support provided by the US Department of Energy (DOE), Office of Science, Office of Basic Energy Sciences, Materials Sciences and Engineering Division and Chemical Sciences, Geosciences, and Biosciences Division at The Pacific Northwest National Laboratory, operated by Battelle for the US Department of Energy (DOE) under Contract DE-AC05-76RL01830. vSFG experiments were performed at the Environmental Molecular Sciences Laboratory (EMSL), a DOE office of Science User Facility sponsored by the Office of Biological and Environmental Research that is located at PNNL.

REFERENCES

(1) Zhao, G.; Jiang, L.; He, Y.; Li, J.; Dong, H.; Wang, X.; Hu, W. Sulfonated Graphene for Persistent Aromatic Pollutant Management. *Adv. Mater.* **2011**, *23* (34), 3959–3963.

(2) Chen, D.; Feng, H.; Li, J. Graphene Oxide: Preparation, Functionalization, and Electrochemical Applications. *Chem. Rev.* **2012**, *112* (11), 6027–6053.

(3) Su, C.; Acik, M.; Takai, K.; Lu, J.; Hao, S.; Zheng, Y.; Wu, P.; Bao, Q.; Enoki, T.; Chabal, Y. J.; Ping Loh, K. Probing the Catalytic Activity of Porous Graphene Oxide and the Origin of This Behaviour. *Nat. Commun.* **2012**, *3* (1), 1298.

(4) Gao, Y.; Li, Y.; Zhang, L.; Huang, H.; Hu, J.; Shah, S. M.; Su, X. Adsorption and Removal of Tetracycline Antibiotics from Aqueous Solution by Graphene Oxide. *J. Colloid Interface Sci.* **2012**, *368* (1), 540–546.

(5) Madadrang, C. J.; Kim, H. Y.; Gao, G.; Wang, N.; Zhu, J.; Feng, H.; Gorring, M.; Kasner, M. L.; Hou, S. Adsorption Behavior of EDTA-Graphene Oxide for Pb (II) Removal. *ACS Appl. Mater. Interfaces* **2012**, *4* (3), 1186–1193.

(6) Dhakshinamoorthy, A.; Alvaro, M.; Concepcion, P.; Fornes, V.; Garcia, H.; Concepción, P.; Fornés, V.; Garcia, H. Graphene Oxide as an Acid Catalyst for the Room Temperature Ring Opening of Epoxides. *Chem. Commun.* **2012**, *48* (44), 5443–5445.

(7) Liu, F.; Chung, S.; Oh, G.; Seo, T. S. Three-Dimensional Graphene Oxide Nanostructure for Fast and Efficient Water-Soluble Dye Removal. *ACS Appl. Mater. Interfaces* **2012**, *4* (2), 922–927.

(8) Huang, H.; Song, Z.; Wei, N.; Shi, L.; Mao, Y.; Ying, Y.; Sun, L.; Xu, Z.; Peng, X. Ultrafast Viscous Water Flow through Nanostrand-Channelled Graphene Oxide Membranes. *Nat. Commun.* **2013**, *4* (1), 2979.

(9) You, S.; Yu, J.; Sundqvist, B.; Belyaeva, L. A.; Avramenko, N. V.; Korobov, M. V.; Talyzin, A. V. Selective Intercalation of Graphite Oxide by Methanol in Water/Methanol Mixtures. *J. Phys. Chem. C* **2013**, *117* (4), 1963–1968.

(10) Romanchuk, A. Y.; Slesarev, A. S.; Kalmykov, S. N.; Kosynkin, D. V.; Tour, J. M. Graphene Oxide for Effective Radionuclide Removal. *Phys. Chem. Chem. Phys.* **2013**, *15* (7), 2321.

(11) DeYoung, A. D.; Park, S.-W.; Dhumal, N. R.; Shim, Y.; Jung, Y.; Kim, H. J. Graphene Oxide Supercapacitors: A Computer Simulation Study. *J. Phys. Chem. C* **2014**, *118* (32), 18472–18480.

(12) Kim, D.; Kim, D. W.; Lim, H.-K.; Jeon, J.; Kim, H.; Jung, H.-T.; Lee, H. Intercalation of Gas Molecules in Graphene Oxide Interlayer: The Role of Water. *J. Phys. Chem. C* **2014**, *118* (20), 11142–11148.

(13) Ban, S.; Jing, X.; Zhou, H.; Zhang, L.; Zhang, J. Experimental and Modeling Study on Charge Storage/Transfer Mechanism of Graphene-Based Supercapacitors. *J. Power Sources* **2014**, *268*, 604–609.

(14) Martins, M. V. A.; Pereira, A. R.; Luz, R. A. S.; Iost, R. M.; Crespilho, F. N. Evidence of Short-Range Electron Transfer of a Redox Enzyme on Graphene Oxide Electrodes. *Phys. Chem. Chem. Phys.* **2014**, *16* (33), 17426–17436.

(15) Smith, Z. P.; Freeman, B. D. Graphene Oxide: A New Platform for High-Performance Gas- and Liquid-Separation Membranes. *Angew. Chemie Int. Ed.* **2014**, *53* (39), 10286–10288.

(16) Gao, W.; Wu, G.; Janicke, M. T.; Cullen, D. A.; Mukundan, R.; Baldwin, J. K.; Brosha, E. L.; Galande, C.; Ajayan, P. M.; More, K. L.; Dattelbaum, A. M.; Zelenay, P. Ozonated Graphene Oxide Film as a Proton-Exchange Membrane. *Angew. Chemie Int. Ed.* **2014**, *53* (14), 3588–3593.

(17) Ray, S. *Applications of Graphene and Graphene-Oxide Based Nanomaterials*; Elsevier, 2015.

(18) Lee, O.-S.; Carignano, M. A. Exfoliation of Electrolyte-Intercalated Graphene: Molecular Dynamics Simulation Study. *J. Phys. Chem. C* **2015**, *119* (33), 19415–19422.

(19) Wang, J.; Chen, B. Adsorption and Coadsorption of Organic Pollutants and a Heavy Metal by Graphene Oxide and Reduced Graphene Materials. *Chem. Eng. J.* **2015**, *281*, 379–388.

(20) Guo, H.; Jiao, T.; Zhang, Q.; Guo, W.; Peng, Q.; Yan, X. Preparation of Graphene Oxide-Based Hydrogels as Efficient Dye Adsorbents for Wastewater Treatment. *Nanoscale Res. Lett.* **2015**, *10* (1), 272.

(21) Xu, Q.; Xu, H.; Chen, J.; Lv, Y.; Dong, C.; Sreeprasad, T. S. Graphene and Graphene Oxide: Advanced Membranes for Gas Separation and Water Purification. *Inorg. Chem. Front.* **2015**, *2* (5), 417–424.

(22) Xu, K.; Ji, X.; Chen, C.; Wan, H.; Miao, L.; Jiang, J. Electrochemical Double Layer near Polar Reduced Graphene Oxide Electrode: Insights from Molecular Dynamic Study. *Electrochim. Acta* **2015**, *166*, 142–149.

(23) Hegab, H. M.; Zou, L. Graphene Oxide-Assisted Membranes: Fabrication and Potential Applications in Desalination and Water Purification. *J. Memb. Sci.* **2015**, *484*, 95–106.

(24) Li, W.; Zheng, X.; Dong, Z.; Li, C.; Wang, W.; Yan, Y.; Zhang, J. Molecular Dynamics Simulations of CO 2 /N 2 Separation through Two-Dimensional Graphene Oxide Membranes. *J. Phys. Chem. C* **2016**, *120* (45), 26061–26066.

(25) Park, S.-W.; DeYoung, A. D.; Dhumal, N. R.; Shim, Y.; Kim, H. J.; Jung, Y. Computer Simulation Study of Graphene Oxide Supercapacitors: Charge Screening Mechanism. *J. Phys. Chem. Lett.* **2016**, *7* (7), 1180–1186.

(26) Abraham, J.; Vasu, K. S.; Williams, C. D.; Gopinadhan, K.; Su, Y.; Cherian, C. T.; Dix, J.; Prestat, E.; Haigh, S. J.; Grigorieva, I. V.; Carbone, P.; Geim, A. K.; Nair, R. R. Tunable Sieving of Ions Using Graphene Oxide Membranes. *Nat. Nanotechnol.* **2017**, *12* (6), 546–550.

(27) Pandey, R. P.; Shukla, G.; Manohar, M.; Shahi, V. K. Graphene Oxide Based Nanohybrid Proton Exchange Membranes for Fuel Cell Applications: An Overview. *Adv. Colloid Interface Sci.* **2017**, *240*, 15–30.

(28) Sun, Y.; Tang, J.; Zhang, K.; Yuan, J.; Li, J.; Zhu, D.-M. M.; Ozawa, K.; Qin, L.-C. C. Comparison of Reduction Products from Graphite Oxide and Graphene Oxide for Anode Applications in Lithium-Ion Batteries and Sodium-Ion Batteries. *Nanoscale* **2017**, *9* (7), 2585–2595.

(29) Thakur, K.; Kandasubramanian, B. Graphene and Graphene Oxide-Based Composites for Removal of Organic Pollutants: A Review. *J. Chem. Eng. Data* **2019**, *64* (3), 833–867.

(30) Chen, Y.; Luo, Z.; Lu, X. Construction of Novel Enzyme–Graphene Oxide Catalytic Interface with Improved Enzymatic Performance and Its Assembly Mechanism. *ACS Appl. Mater. Interfaces* **2019**, *11* (12), 11349–11359.

(31) Witomska, S.; Liu, Z.; Czepa, W.; Aliprandi, A.; Pakulski, D.; Pawluć, P.; Ciesielski, A.; Samorì, P. Graphene Oxide Hybrid with Sulfur–Nitrogen Polymer for High-Performance Pseudocapacitors. *J. Am. Chem. Soc.* **2019**, *141* (1), 482–487.

(32) Dong, Y.; Cheng, Y.; Xu, G.; Cheng, H.; Huang, K.; Duan, J.; Mo, D.; Zeng, J.; Bai, J.; Sun, Y.; Liu, J.; Yao, H. Selectively Enhanced Ion Transport in Graphene Oxide Membrane/PET Conical Nanopore System. *ACS Appl. Mater. Interfaces* **2019**, *11* (16), 14960–14969.

(33) Yang, H.; Yeow, B. S.; Chang, T.-H.; Li, K.; Fu, F.; Ren, H.; Chen, P.-Y. Graphene Oxide-Enabled Synthesis of Metal Oxide Origamis for Soft Robotics. *ACS Nano* **2019**, *13* (5), 5410–5420.

(34) Qiu, R.; Yuan, S.; Xiao, J.; Chen, X. D.; Selomulya, C.; Zhang, X.; Woo, M. W. Effects of Edge Functional Groups on Water Transport in Graphene Oxide Membranes. *ACS Appl. Mater. Interfaces* **2019**, *11* (8), 8483–8491.

(35) Yoon, H. W.; Lee, T. H.; Doherty, C. M.; Choi, T. H.; Roh, J. S.; Kim, H. W.; Cho, Y. H.; Do, S.; Freeman, B. D.; Park, H. B. Origin of CO 2 -Philic Sorption by Graphene Oxide Layered Nanosheets and Their Derivatives. *J. Phys. Chem. Lett.* **2020**, *11* (6), 2356–2362.

(36) Garg, B.; Bisht, T.; Ling, Y.-C. Graphene-Based Nanomaterials as Heterogeneous Acid Catalysts: A Comprehensive Perspective. *Molecules* **2014**, *19* (9), 14582–14614.

(37) He, H.; Klinowski, J.; Forster, M.; Lerf, A. A New Structural Model for Graphite Oxide. *Chem. Phys. Lett.* **1998**, *287* (1–2), 53–56.

(38) Lerf, A.; He, H.; Forster, M.; Klinowski, J. Structure of Graphite Oxide Revisited. *J. Phys. Chem. B* **1998**, *102* (23), 4477–4482.

(39) Lerf, A.; He, H.; Riedl, T.; Forster, M.; Klinowski, J. 13C and 1H MAS NMR Studies of Graphite Oxide and Its Chemically Modified Derivatives. *Solid State Ionics* **1997**, *101–103*, 857–862.

(40) Motevalli, B.; Parker, A. J.; Sun, B.; Barnard, A. S. The Representative Structure of Graphene Oxide Nanoflakes from Machine Learning. *Nano Futur.* **2019**, *3* (4).

(41) Sinclair, R. C.; Coveney, P. V. Modeling Nanostructure in Graphene Oxide: Inhomogeneity and the Percolation Threshold. *J. Chem. Inf. Model.* **2019**, *59* (6), 2741–2745.

(42) Zaera, F. Probing Liquid/Solid Interfaces at the Molecular Level. *Chem. Rev.* **2012**, *112* (5), 2920–2986.

(43) Flynn Bolte, K. T.; Balaraman, R. P.; Jiao, K.; Tustison, M.; Kirkwood, K. S.; Zhou, C.; Kohli, P. Probing Liquid–Solid and Vapor–Liquid–Solid Interfaces of Hierarchical Surfaces Using High-Resolution Microscopy. *Langmuir* **2018**, *34* (12), 3720–3730.

(44) Woodruff, D. P.; Delchar, T. A. *Modern Techniques of Surface Science*; Cambridge University Press: Cambridge, 1994.

(45) Turner, N. H.; Dunlap, B. I.; Colton, R. J. Surface Analysis: X-Ray Photoelectron Spectroscopy, Auger Electron Spectroscopy and Secondary Ion Mass Spectrometry. *Anal. Chem.* **1984**, *56* (5), 373–416.

(46) Belsey, N. A.; Shard, A. G.; Minelli, C. Surface Chemistry. In *Nanomaterial Characterization*; John Wiley & Sons, Inc: Hoboken, NJ, USA, 2016; pp 153–178.

(47) Hunt, J. H.; Guyot-Sionnest, P.; Shen, Y. R. Observation of C-H Stretch Vibrations of Monolayers of Molecules Optical Sum-Frequency Generation. *Chem. Phys. Lett.* **1987**, *133* (3), 189–192.

(48) Guyot-Sionnest, P.; Hunt, J. H.; Shen, Y. R. Sum-Frequency Vibrational Spectroscopy of a Langmuir Film: Study of Molecular Orientation of a Two-Dimensional System. *Phys. Rev. Lett.* **1987**, *59* (14), 1597–1600.

(49) Stiopkin, I. V.; Jayathilake, H. D.; Bordenyuk, A. N.; Benderskii, A. V. Heterodyne-Detected Vibrational Sum Frequency Generation Spectroscopy. *J. Am. Chem. Soc.* **2008**, *130* (7), 2271–2275.

(50) Nihonyanagi, S.; Yamaguchi, S.; Tahara, T. Direct Evidence for Orientational Flip-Flop of Water Molecules at Charged Interfaces: A Heterodyne-Detected Vibrational Sum Frequency Generation Study. *J. Chem. Phys.* **2009**, *130* (20), 204704.

(51) Nagata, Y.; Hsieh, C.-S.; Hasegawa, T.; Voll, J.; Backus, E. H. G.; Bonn, M. Water Bending Mode at the Water–Vapor Interface Probed by Sum-Frequency Generation Spectroscopy: A Combined Molecular Dynamics Simulation and Experimental Study. *J. Phys. Chem. Lett.* **2013**, *4* (11), 1872–1877.

(52) Perakis, F.; De Marco, L.; Shalit, A.; Tang, F.; Kann, Z. R.; Kühne, T. D.; Torre, R.; Bonn, M.; Nagata, Y. Vibrational Spectroscopy and Dynamics of Water. *Chem. Rev.* **2016**, *116* (13), 7590–7607.

(53) Balzerowski, P.; Meister, K.; Versluis, J.; Bakker, H. J. Heterodyne-Detected Sum Frequency Generation Spectroscopy of Polyacrylic Acid at the Air/Water-Interface. *Phys. Chem. Chem. Phys.* **2016**, *18* (4), 2481–2487.

(54) Singla, S.; Anim-Danso, E.; Islam, A. E.; Ngo, Y.; Kim, S. S.; Naik, R. R.; Dhinojwala, A. Insight on Structure of Water and Ice Next to Graphene Using Surface-Sensitive Spectroscopy. *ACS Nano* **2017**, *11* (5), 4899–4906.

(55) Wilson, M. C.; Singla, S.; Stefin, A. J.; Kaur, S.; Brown, J. V.; Dhinojwala, A. Characterization of Acid–Base Interactions Using Interface-Sensitive Sum Frequency Generation Spectroscopy. *J. Phys. Chem. C* **2019**, *123* (30), 18495–18501.

(56) Link, K. A.; Spurzem, G. N.; Tuladhar, A.; Chase, Z.; Wang, Z.; Wang, H.; Walker, R. A. Organic Enrichment at Aqueous Interfaces: Cooperative Adsorption of Glucuronic Acid to DPPC Monolayers Studied with Vibrational Sum Frequency Generation. *J. Phys. Chem. A* **2019**, *123* (26), 5621–5632.

(57) Tuladhar, A.; Chase, Z. A.; Baer, M. D.; Legg, B. A.; Tao, J.; Zhang, S.; Winkelman, A. D.; Wang, Z.; Mundy, C. J.; De Yoreo, J. J.; Wang, H. Direct Observation of the Orientational Anisotropy of Buried Hydroxyl Groups inside Muscovite Mica. *J. Am. Chem. Soc.* **2019**, *141* (5), 2135–2142.

(58) Morita, A.; Ishiyama, T. Recent Progress in Theoretical Analysis of Vibrational Sum Frequency Generation Spectroscopy. *Phys. Chem. Chem. Phys.* **2008**, *10* (38), 5801.

(59) Auer, B. M.; Skinner, J. L. Vibrational Sum-Frequency Spectroscopy of the Liquid/Vapor Interface for Dilute HOD in D2O. *J. Chem. Phys.* **2008**, *129* (21), 214705.

(60) Sulpizi, M.; Salanne, M.; Sprik, M.; Gaigeot, M.-P. Vibrational Sum Frequency Generation Spectroscopy of the Water Liquid–Vapor Interface from Density Functional Theory-Based Molecular Dynamics Simulations. *J. Phys. Chem. Lett.* **2013**, *4* (1), 83–87.

(61) Kishinaka, S.; Morita, A.; Ishiyama, T. Molecular Structure and Vibrational Spectra at Water/Poly(2-Methoxyethylacrylate) and Water/Poly(Methyl Methacrylate) Interfaces: A Molecular Dynamics Simulation Study. *J. Chem. Phys.* **2019**, *150* (4), 044707.

(62) Tuladhar, A.; Dewan, S.; Pezzotti, S.; Brigiano, F. S.; Creazzo, F.; Gaigeot, M.-P.; Borguet, E. Ions Tune Interfacial Water Structure and Modulate Hydrophobic Interactions at Silica Surfaces. *J. Am. Chem. Soc.* **2020**, jacs.9b13273.

(63) Martínez, L.; Andrade, R.; Birgin, E. G.; Martínez, J. M. PACKMOL: A Package for Building Initial Configurations for Molecular Dynamics Simulations. *J. Comput. Chem.* **2009**, *30* (13), 2157–2164.

(64) Jewett, A. I.; Zhuang, Z.; Shea, J.-E. Moltemplate a Coarse-Grained Model Assembly Tool. *Biophys. J.* **2013**, *104* (2), 169a.

(65) Jorgensen, W. L.; Maxwell, D. S.; Tirado-Rives, J. Development and Testing of the OPLS All-Atom Force Field on Conformational Energetics and Properties of Organic Liquids. *J. Am. Chem. Soc.* **1996**, *118* (45), 11225–11236.

(66) Berendsen, H. J. C.; Grigera, J. R.; Straatsma, T. P. The Missing Term in Effective Pair Potentials. *J. Phys. Chem.* **1987**, *91* (24), 6269–6271.

(67) Hockney, R. .; Eastwood, J. . *Computer Simulation Using Particles*; Taylor & Francis, 1988.

(68) Ryckaert, J.-P.; Ciccotti, G.; Berendsen, H. J. . Numerical Integration of the Cartesian Equations of Motion of a System with Constraints: Molecular Dynamics of n-Alkanes. *J. Comput. Phys.* **1977**, *23* (3), 327–341.

(69) Nosé, S. A Molecular Dynamics Method for Simulations in the Canonical Ensemble. *Mol. Phys.* **1984**, *52* (2), 255–268.

(70) Hoover, W. G. Canonical Dynamics: Equilibrium Phase-Space Distributions. *Phys. Rev. A* **1985**, *31* (3), 1695–1697.

(71) VandeVondele, J.; Krack, M.; Mohamed, F.; Parrinello, M.; Chassaing, T.; Hutter, J. Quickstep: Fast and Accurate Density Functional Calculations Using a Mixed Gaussian and Plane Waves Approach. *Comput. Phys. Commun.* **2005**, *167* (2), 103–128.

(72) Hutter, J.; Iannuzzi, M.; Schiffmann, F.; VandeVondele, J. Cp2k: Atomistic Simulations of Condensed Matter Systems. *Wiley Interdiscip. Rev. Comput. Mol. Sci.* **2014**, *4* (1), 15–25.

(73) Byrd, R. H.; Lu, P.; Nocedal, J.; Zhu, C. A Limited Memory Algorithm for Bound Constrained Optimization. *SIAM J. Sci. Comput.* **1995**, *16* (5), 1190–1208.

(74) Perdew, J. P.; Burke, K.; Ernzerhof, M. Generalized Gradient Approximation Made Simple. *Phys. Rev. Lett.* **1996**, *77* (18), 3865–3868.

(75) Zhang, Y.; Yang, W. Comment on "Generalized Gradient Approximation Made Simple." *Phys. Rev. Lett.* **1998**, *80* (4), 890–890.

(76) Grimme, S.; Antony, J.; Ehrlich, S.; Krieg, H. A Consistent and Accurate Ab Initio Parametrization of Density Functional Dispersion Correction (DFT-D) for the 94 Elements H-Pu. *J. Chem. Phys.* **2010**, *132* (15), 154104.

(77) VandeVondele, J.; Hutter, J. Gaussian Basis Sets for Accurate Calculations on Molecular Systems in Gas and Condensed Phases. *J. Chem. Phys.* **2007**, *127* (11), 114105.

(78) Goedecker, S.; Teter, M.; Hutter, J. Separable Dual-Space Gaussian Pseudopotentials. *Phys. Rev. B* **1996**, *54* (3), 1703–1710.

(79) Hartwigsen, C.; Goedecker, S.; Hutter, J. Relativistic Separable Dual-Space Gaussian Pseudopotentials from H to Rn. *Phys. Rev. B* **1998**, *58* (7), 3641–3662.

(80) Krack, M. Pseudopotentials for H to Kr Optimized for Gradient-Corrected Exchange-Correlation Functionals. *Theor. Chem. Acc.* **2005**, *114* (1–3), 145–152.

(81) Bussi, G.; Donadio, D.; Parrinello, M. Canonical Sampling through Velocity Rescaling. *J. Chem. Phys.* **2007**, *126* (1), 014101.

(82) Lu, Z.; Karakoti, A.; Velarde, L.; Wang, W.; Yang, P.; Thevuthasan, S.; Wang, H. Dissociative Binding of Carboxylic Acid Ligand on Nanoceria Surface in Aqueous Solution: A Joint In Situ Spectroscopic Characterization and First-Principles Study. *J. Phys. Chem. C* **2013**, *117* (46), 24329–24338.

(83) Lu, R.; Gan, W.; Wu, B.; Chen, H.; Wang, H. Vibrational Polarization Spectroscopy of CH Stretching Modes of the Methylene Group at the Vapor/Liquid Interfaces with Sum Frequency Generation. *J. Phys. Chem. B* **2004**, *108* (22), 7297–7306.

(84) Ohto, T.; Usui, K.; Hasegawa, T.; Bonn, M.; Nagata, Y. Toward Ab Initio Molecular Dynamics Modeling for Sum-Frequency Generation Spectra; an Efficient Algorithm Based on Surface-Specific Velocity-Velocity Correlation Function. *J. Chem. Phys.* **2015**, *143* (12), 124702.

(85) Mukamel, S. *Principles of Nonlinear Optical Spectroscopy*; Oxford series in optical and imaging sciences; Oxford University Press, 1999.

(86) Liu, J.; Miller, W. H.; Paesani, F.; Zhang, W.; Case, D. A. Quantum Dynamical Effects in Liquid Water: A Semiclassical Study on the Diffusion and the Infrared Absorption Spectrum. *J. Chem. Phys.* **2009**, *131* (16), 164509.

(87) Berens, P. H.; Wilson, K. R. Molecular Dynamics and Spectra. I. Diatomic Rotation and Vibration. *J. Chem. Phys.* **1981**, *74* (9), 4872–4882.

(88) Corcelli, S. A.; Skinner, J. L. Infrared and Raman Line Shapes of Dilute HOD in Liquid H 2O and D 2O from 10 to 90°C. *J. Phys. Chem. A* **2005**, *109* (28), 6154–6165.

(89) Auer, B. M.; Skinner, J. L. IR and Raman Spectra of Liquid Water: Theory and Interpretation. *J. Chem. Phys.* **2008**, *128* (22), 224511.

(90) Willard, A. P.; Chandler, D. Instantaneous Liquid Interfaces. *J. Phys. Chem. B* **2010**, *114* (5), 1954–1958.

(91) Serva, A.; Pezzotti, S.; Bougueroua, S.; Galimberti, D. R.; Gaigeot, M.-P. Combining Ab-Initio and Classical Molecular Dynamics Simulations to Unravel the Structure of the 2D-HB-Network at the Air-Water Interface. *J. Mol. Struct.* **2018**, *1165*, 71–78.

(92) Pezzotti, S.; Galimberti, D. R.; Shen, Y. R.; Gaigeot, M.-P. Structural Definition of the BIL and DL: A New Universal Methodology to Rationalize Non-Linear χ (2) (ω) SFG Signals at Charged Interfaces, Including χ (3) (ω) Contributions. *Phys. Chem. Chem. Phys.* **2018**, *20* (7), 5190–5199.

(93) Auer, B.; Kumar, R.; Schmidt, J. R.; Skinner, J. L. Hydrogen Bonding and Raman, IR, and 2D-IR Spectroscopy of Dilute HOD in Liquid D2O. *Proc. Natl. Acad. Sci.* **2007**, *104* (36), 14215–14220.

(94) Richmond, G. L. Molecular Bonding and Interactions at Aqueous Surfaces as Probed by Vibrational Sum Frequency Spectroscopy. *Chem. Rev.* **2002**, *102* (8), 2693–2724.

(95) Joutsuka, T.; Hirano, T.; Sprik, M.; Morita, A. Effects of Third-Order Susceptibility in Sum Frequency Generation Spectra: A Molecular Dynamics Study in Liquid Water. *Phys. Chem. Chem. Phys.* **2018**, *20* (5), 3040–3053.

(96) Ohno, P. E.; Wang, H.; Paesani, F.; Skinner, J. L.; Geiger, F. M. Second-Order Vibrational Lineshapes from the Air/Water Interface. *J. Phys. Chem. A* **2018**, *122* (18), 4457–4464.

(97) Morita, A.; Hynes, J. T. A Theoretical Analysis of the Sum Frequency Generation Spectrum of the Water Surface. II. Time-Dependent Approach. *J. Phys. Chem. B* **2002**, *106* (3), 673–685.

(98) Nihonyanagi, S.; Mondal, J. A.; Yamaguchi, S.; Tahara, T. Structure and Dynamics of Interfacial Water Studied by Heterodyne-Detected Vibrational Sum-Frequency Generation. *Annu. Rev. Phys. Chem.* **2013**, *64* (1), 579–603.

(99) Ji, N.; Ostroverkhov, V.; Tian, C. S.; Shen, Y. R. Characterization of Vibrational Resonances of Water-Vapor Interfaces by Phase-Sensitive Sum-Frequency Spectroscopy. *Phys. Rev. Lett.* **2008**, *100* (9), 096102.

(100) Ohto, T.; Tada, H.; Nagata, Y. Structure and Dynamics of Water at Water–Graphene and Water–Hexagonal Boron-Nitride Sheet Interfaces Revealed by Ab Initio Sum-Frequency Generation Spectroscopy. *Phys. Chem. Chem. Phys.* **2018**, *20* (18), 12979–12985.

(101) Wen, Y.-C.; Zha, S.; Tian, C.; Shen, Y. R. Surface PH and Ion Affinity at the Alcohol-Monolayer/Water Interface Studied by Sum-Frequency Spectroscopy. *J. Phys. Chem. C* **2016**, *120* (28), 15224–15229.

(102) Reddy, S. K.; Thiraux, R.; Wellen Rudd, B. A.; Lin, L.; Adel, T.; Joutsuka, T.; Geiger, F. M.; Allen, H. C.; Morita, A.; Paesani, F. Bulk Contributions Modulate the Sum-Frequency Generation Spectra of Water on Model Sea-Spray Aerosols. *Chem* **2018**, *4* (7), 1629–1644.

(103) Moberg, D. R.; Li, Q.; Reddy, S. K.; Paesani, F. Water Structure at the Interface of Alcohol Monolayers as Determined by Molecular Dynamics Simulations and Computational Vibrational Sum-Frequency Generation Spectroscopy. *J. Chem. Phys.* **2019**, *150* (3), 034701.

(104) Lu, R.; Gan, W.; Wu, B.; Zhang, Z.; Guo, Y.; Wang, H. C−H Stretching Vibrations of Methyl, Methylene and Methine Groups at the Vapor/Alcohol (n = 1−8) Interfaces. *J. Phys. Chem. B* **2005**, *109* (29), 14118–14129.

(105) Xu, J.; Chen, M.; Zhang, C.; Wu, X. First-Principles Study of the Infrared Spectrum in Liquid Water from a Systematically Improved Description of H-Bond Network. *Phys. Rev. B* **2019**, *99* (20), 205123.

(106) Tuladhar, A.; Dewan, S.; Kubicki, J. D.; Borguet, E. Spectroscopy and Ultrafast Vibrational Dynamics of Strongly Hydrogen Bonded OH Species at the α-Al 2 O 3 (11$\bar{2}$0)/H 2 O Interface. *J. Phys. Chem. C* **2016**, *120* (29), 16153–16161.

(107) Sulpizi, M.; Gaigeot, M.-P.; Sprik, M. The Silica–Water Interface: How the Silanols Determine the Surface Acidity and Modulate the Water Properties. *J. Chem. Theory Comput.* **2012**, *8* (3), 1037–1047.

(108) Gaigeot, M.-P.; Sprik, M.; Sulpizi, M. Oxide/Water Interfaces: How the Surface Chemistry Modifies Interfacial Water Properties. *J. Phys. Condens. Matter* **2012**, *24* (12), 124106.

(109) Ishiyama, T.; Imamura, T.; Morita, A. Theoretical Studies of Structures and Vibrational Sum Frequency Generation Spectra at Aqueous Interfaces. *Chem. Rev.* **2014**, *114* (17), 8447–8470.